Proceedings of the 7th International Symposium on Cavitation
CAV2009
August 16-22, 2009, Ann Arbor, Michigan, USA

CAV2009 Paper No. 74

A HYBRID LAGRANGIAN-EULERIAN APPROACH FOR SIMULATION OF BUBBLE DYNAMICS

Sourabh V. Apte[*], **Ehsan Shams, and Justin Finn**
Computational Flow Physics Laboratory
School of Mechanical Industrial and Manufacturing Engineering
Oregon State University, 204 Rogers Hall, Corvallis, OR 97331
Email: sva@engr.orst.edu, WWW: http://web.engr.oregonstate.edu/ sva/

ABSTRACT

A mutiscale numerical approach is developed for the investigation of bubbly flows in turbulent environments. This consists of two different numerical approaches capable of capturing the bubble dynamics at different scales depending upon the relative size of the bubbles compared to the grid resolution: (i) fully resolved simulations (FRS) wherein the bubble dynamics and deformation are completely resolved, and (ii) subgrid, discrete bubble model where the bubbles are not resolved by the computational grid. For fully resolved simulations, a novel approach combining a particle-based, mesh-free technique with a finite-volume flow solver, is developed. The approach uses marker points around the interface and advects the signed distance to the interface in a Lagrangian frame. Interpolation kernel based derivative calculations typical of particle methods are used to extract the interface normal and curvature from unordered marker points. Unlike front-tracking methods, connectivity between the marker points is not necessary. For under-resolved bubbles, a mixture-theory based Eulerian-Lagrangian approach accounting for volumetric displacements due to bubble motion and size variations is developed. The bubble dynamics is modeled by Rayleigh-Plesset equations using an adaptive time-stepping scheme. A detailed verification and validation study of both approaches is performed to test the accuracy of the method on a variety of single and multiple bubble problems to show good predictive capability. Interaction of bubbles with a traveling vortex tube is simulated and compared with experimental data of Sridhar and Katz [1] to show good agreement.

1 INTRODUCTION

Two-phase flows with phase change occur in many engineering systems. Of specific interest are two applications involving wide range of length and time scales: (a) bubbly turbulent flows in the ship boundary layers for drag reduction and (b) hydrodynamics of cavitation. These problems share common physical mechanisms of mass, momentum, and energy exchange across the interface between the two phases. The dispersed bubbles may deform, vary in size, or coalesce and the local grid resolution may be such that the bubble is fully resolved or under-resolved in relation to the resolution of the background mesh (see Figure 1). In cavitating flows, the vapor cavity size can change dynamically and the the local grid resolution may be such that the

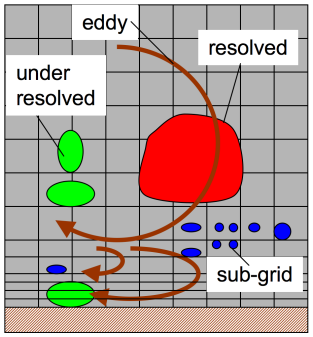

Figure 1: A schematic of the need for multiscale simulation strategy showing fully resolved and under-resolved bubbles.

[*]Address all correspondence to this author.

cavity (or bubbles) are fully (or partially) resolved on the grid or completely sub-grid. Different approaches are needed to model these flow regimes accurately. It is essential to develop mathematical formulation and supporting numerical schemes that can accurately and simultaneously model the motion of sub-grid, partially, or fully resolved bubbles. In addition, predictive simulations of turbulent flows in realistic flow configurations makes it imperative to resort to large-eddy simulations (LES). It is thus necessary to develop numerical models for two-phase flows that can be applied to LES of complex flows.

In this work, two approaches are described for bubbly flow simulations: (i) a new Eulerian-Lagrangian particle-based method for fully resolved simulations, and (ii) a subgrid-scale discrete-bubble model for large-eddy simulation of under-resolved bubbles. The hybrid Eulerian-Lagrangian approach combines grid-based finite-volume solver [2,3] with a mesh-free, marker particle-based approach for interface tracking without requiring inter-particle connectivity information. For bubbles that are under-resolved or are subgrid, a discrete bubble model with Rayleigh-Plesset equation for bubble dynamics is used. The bubbles and the liquid phase are treated by mixture theory based equations [4].

The paper is arranged as follows. Details of the fully-resolved simulation methodology, numerical algorithm, and validation test cases are provided in section 2. The sub-grid scale discrete-bubble model, the adaptive time-stepping approach, and validation of the model is described in section 3. Finally, interaction of the rising bubbles in a traveling vortex based on the experimental study of Sridhar and Katz [1] is presented in section 4.

2 FULLY RESOLVED SIMULATIONS

Numerical methods to accurately track/capture the interface between two fluids have been an area of research for decades. Tryggvason *et al.* [5] provide a detailed review on various methods used for direct simulation of multiphase flows. Broadly, these schemes can be classified into two categories: (a) front tracking and (b) front capturing methods. Front tracking methods are Lagrangian in nature and the interface is tracked by a set of connected [5] or unconnected [6] marker points on the interface and the Navier-Stokes equations are solved on a fixed grid in an Eulerian frame.

In capturing methods the interface is not explicitly tracked, but captured using a characteristic function, which evolves using the advection equation. Representative capturing methods are: volume tracking [7], level set [8,9] and phase field models. Both approaches (the VoF and level set) are straightforward to implement, however, level-set approach does not preserve volume of the fluids on either side of the interface. The VOF formulation on the other hand, conserves the fluid volume but lacks in the sharpness of the interface. Several improvements to these methods involving combination of the two [10,11], particle-level sets [12], refined level-set grid scheme [13], have been proposed for improved accuracy.

Pure mesh-free approaches have also been used for fully resolved simulations involving deforming interfaces. These particle-based methods such as smoothed-particle hydrodynamics (SPH) [14] and remeshed-SPH methods [15, 16] have been popular for large-scale free-surface flows.

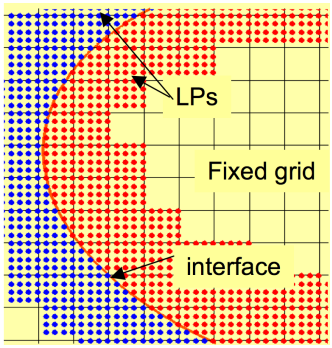

Figure 2: Marker points for interface location.

In the present work, a new hybrid approach is developed wherein the Lagrangian nature of the interface motion is captured by particle-based method, and the fluid flow is computed using a finite-volume solver using variable density, single-fluid model. The basic idea is to merge the locally 'adaptive' mesh-free particle-based methods with the relative 'ease' of Eulerian finite-volume formulation in order to inherit the advantages offered by individual approaches. The interface between two fluids is represented and tracked using Lagrangian points (LPs) or fictitious particles [16] that are uniformly spaced in a narrow band around the interface as shown in Figure 2. Each LP is associated with position $\mathbf{x}_p$, velocity $\mathbf{u}_p$, volume $\mathcal{V}_p$ and a scalar function Φ_p which represents the signed distance to the interface. Unlike particle level set method [12] or the semi-Lagrangian methods [17], in the present approach the interface is advected in a Lagrangian frame. The motion of the interface is determined by a velocity field (interpolated to the particle locations) obtained by solving the Navier-Stokes equations on a *fixed* background mesh in an Eulerian frame. The interface location, once determined, identifies the region of the mesh to apply *jump-conditions* in fluid properties. The potential advantage of the present hybrid method is that the background mesh could be of any kind: *structured, body-fitted, or arbitrary shaped unstructured* (hex, pyramids, tetrahedrons, prisms) and may be *stationary or changing in time (adaptive refinement)*. As the first step, flows where thermal effects are negligible are considered. A single fluid formulation based on a co-located grid, unstructured grid finite-volume solver is developed for simulation of the unsteady viscous flow inside and outside the bubbles.

The average spacing (h) between the uniformly spaced LPs is related to the volume $\mathcal{V}_p$. In this work, LPs with cubic elements ($h = \mathcal{V}_p^{1/3}$) are used. As the LPs move, they carry the signed distance function (*SDF*) value along the characteristic paths and implicitly represent the motion of the interface. The evolution of the interface is calculated by solving level set equations in the Lagrangian form:

$$\frac{D\Phi_p}{Dt} = 0;\ \frac{D\mathcal{V}_p}{Dt} = \langle \nabla \cdot \mathbf{u} \rangle_p \mathcal{V}_p;\ \frac{D\mathbf{x}_p}{Dt} = \mathbf{u}_p, \tag{1}$$

where p denotes the Lagrangian point or particle. As is done in Smoothed Particle Hydrodynamics (SPH) and mesh-free methods, smoothed approximation of the level set function and its derivatives can be obtained by using a mollification operator with LPs as quadrature points. The localized mollification kernel (ξ_ε) generates a smooth continuous approximation of Φ around the LP at location $\mathbf{x}_p$ using SDF at other LP locations $\mathbf{x}_q$: $\Phi_q = \sum_{p=1}^{N} \mathcal{V}_p \Phi_p \xi_\varepsilon(\mathbf{x}_q - \mathbf{x}_p)$ where $\Phi_q = \Phi(\mathbf{x}_q)$ and $\sum_{p=1}^{N} \xi_\varepsilon \mathcal{V}_p = 1$. In this work a quartic spline is used for mollification:

$$\xi_\varepsilon(\mathbf{x}) = \begin{cases} \frac{s^4}{4} - \frac{5s^2}{8} + \frac{115}{192}, & 0 \le s < \frac{1}{2} \\ -\frac{s^4}{6} + \frac{5s^3}{6} - \frac{5s^2}{4} + \frac{5s}{24} + \frac{55}{96} & \frac{1}{2} \le s < \frac{3}{2} \\ \frac{(2.5-s)^4}{24}, & \frac{3}{2} \le s < \frac{5}{2} \\ 0 & s \ge \frac{5}{2} \end{cases}$$

where $s = |\mathbf{x}|/\varepsilon$. Here, ε is the radius of influence around the LP and depends on the spacing between the LPs and the width of the mollification kernel. For all calculations in this work ε is set equal to the uniform spacing between the LPs. The surface normal and curvature calculations require derivatives of the scalar function Φ on the particles. These are approximated by using derivatives of the quartic spline kernels in a form that conserves higher-order moments [18].

$$\langle \nabla \Phi \rangle_q = \sum_p \mathcal{V}_p (\Phi_p - \Phi_q) \nabla \xi_\varepsilon(\mathrm{x}_q - \mathrm{x}_p), \tag{2}$$

$$\langle \nabla^2 \Phi \rangle_q = \sum_p \mathcal{V}_p (\Phi_p - \Phi_q) \nabla^2 \xi_\varepsilon(\mathrm{x}_q - \mathrm{x}_p). \tag{3}$$

These mollification operations require information about the neighboring LPs inside the region of influence, and a Verlet list and linked lists are used to optimize storage and location of the neighbors.

Once the location of the LPs and the associated Φ_p values are obtained, a color function $\Theta(\mathbf{x})$ can be constructed. Following the definition of color function, finding Θ on the LPs is straightforward: $\Theta = 0$ when $\Phi \ge 0$ and $\Theta = 1$ for $\Phi < 0$. Then the color function field can also be obtained on the background computational mesh by interpolating Θ from the LPs. In order to obtain a smooth function, the M_4' kernel interpolation in three-dimensions is used [16]. Once the color function (or void fraction) Θ is obtained at a control volume (*cv*), the density and viscosity are given as:

$$\rho_{cv} = \rho_g + (\rho_\ell - \rho_g)\Theta_{cv}; \quad \mu_{cv} = \mu_g + (\mu_\ell - \mu_g)\Theta_{cv} \tag{4}$$

where subscripts ℓ and g stand for liquid and gas, respectively. The flow field is computed on a background mesh (which could be structured or unstructured) by solving the Navier-Stokes equations:

$$\nabla \cdot \mathbf{u} = 0;\ \ \frac{\partial \mathbf{u}}{\partial t} + \mathbf{u} \cdot \nabla \mathbf{u} = -\frac{1}{\rho}\nabla p + \frac{1}{\rho}\nabla \cdot (\mu(\nabla \mathbf{u} + (\nabla \mathbf{u})^T)) + \mathbf{g} + \frac{1}{\rho}\mathbf{F}_\sigma \tag{5}$$

where $\mathbf{u}$ is velocity vector of fluid, p is pressure, ρ and μ are fluid density and viscosity (uniform inside each fluid), $\mathbf{g}$ body force, and $\mathbf{F}_\sigma$ is the surface tension force which is non-zero only at the interface location ($\Phi = 0$). Following Brackbill *et al.* [19], the surface tension force is modeled as a continuum surface force (CSF). A common issue with numerical simulations involving surface tension force, is the development of *spurious currents* (unphysical velocity field) [5] due to inaccuracies in the discrete approximations to the surface-tension forces (equation 5). In order to obtain a consistent coupling of the surface tension force with the pressure gradient forces in a finite-volume approach, Francois *et al.* [20] indicated that the surface tension force must be evaluated at the faces of the control volumes as: $\mathbf{F}_{\sigma,f}^{CSF} = \sigma \kappa_f (\nabla \Theta)_f$ where the subscript f stands for the face of the control volume, σ is the surface tension coefficient (assumed constant in the present work), κ is the curvature, $\hat{\mathbf{n}}$ the interface normal. The surface tension force at the *cv*-centers can be obtained through reconstruction from the faces of each *cv*.

To compute the surface tension force, accurate estimation of the curvature of the interface is necessary. Herrmann [13] developed a procedure to compute the curvature accurately in the level-set framework. A similar procedure for curvature evaluations if used. First, the curvature and normals ($\kappa = \nabla \cdot (\frac{\nabla \Phi}{|\nabla \Phi|}); \mathbf{n} = \frac{\nabla \Phi}{|\nabla \Phi|}$) are evaluated at the LPs close to the interface ($|\Phi| \le 2\Delta_{LP}$, where Δ_{LP} is the spacing between the LPs. The gradients in the curvature and surface normal computations are evaluated from derivatives of the mollification kernels. For each of these LPs (with $|\Phi| \le 2\Delta_{LP}$), a base point on the interface is obtained by projecting normals onto the interface. Curvature on the base point is evaluated by using curvature values on LPs in its neighborhood using the M_4'-kernel based interpolation. Once curvatures on all interface points are evaluated, these values are *assigned* to the corresponding LPs from which these interface points were obtained. Curvature at the background control volume *cv* is then computed by using surface averaging of the curvatures of LPs that lie inside the control volume. Curvature at

the faces of the control volume are evaluated by arithmetic average of the two control volumes associated with the face. Here, the average is taken only if the both *cv*s contain the interface, i.e. color function $0 < \Theta_{cv} < 1$, else κ_f is assigned the value of κ_{cv} containing the interface.

2.1 Numerical Algorithm for Resolved Simulation

The governing equations are solved using a co-located grid finite-volume algorithm [21]. Accordingly, all variables are stored at the control volume (*cv*) centers with the exception of a face-normal velocity, located at the face centers, and used to enforce the divergence-free constraint. The variables are staggered in time so that they are located most conveniently for the time advancement scheme. Knowing the velocity field at the *cv* centers, it is interpolated to the particle locations using the quartic spline kernel. The LPs are then advanced by solving the equations 1 using a third-order Runge-Kutta scheme. The LPs are re-located and duly transferred to different processors.

Because of this advection, the original uniform map of LPs may get distorted, and they are reconfigured (if a threshold distortion is exceeded) to a uniform Cartesian lattice. This process of remeshing or reconfiguration was introduced in Remeshed-Smoothed Particle Hydrodynamics [15]. Remeshing removes any unphysical kinks in the interface and gives 'entropy-satisfying viscous solution' [16]. It also eliminates unnecessary points away from the interface. The M_4' kernel is used to obtain the interpolated SDF values during remeshing. Although the reconfiguration procedure provides the entropy solution, it does not guarantee that Φ remains a signed-distance to the interface. We apply redistancing in a two-layer narrow band around the interface [22] in which the solved on uniformly spaced LPs [23]: $\frac{\partial \Phi}{\partial \tau} = \text{sign}(\Phi_0)(1 - |\nabla \Phi|)$ where $\Phi(x,0) = \Phi_0$ and $\text{sign}(\Phi_0) \equiv 2(H_\varepsilon(\Phi) - 1/2)$ and $H_\varepsilon(\Phi)$ is the Heaviside function.

Once the new LP locations are obtained, interface properties such as curvature, surface normal are obtained by using conservative formulation based on the derivatives of the kernel functions. The curvatures at the cv-centers and a color function are obtained as described in the previous section. The two-phase flow properties are then evaluated at the *cv* centers, and the Navier-Stokes equations are solved using the balanced force algorithm [13, 20] that enforces discrete balance of surface tension force and pressure gradient in the absence of any flow and other external forces. The basic steps are summarized below:

1. Advance the LPs (from $t^{n-1/2}$ to $t^{n+1/2}$) according to equations (1) and using a velocity field interpolated to the LP location from the background mesh. Third-order Runge-Kutta scheme is used to solve the ordinary differential equations for each LP.

2. Remesh and reinitialize the particle-map if necessary. Remeshing of LPs is necessary only if the particles cease to overlap as they adapt to the flow map. Reinitialization is only necessary after a few remeshing steps.

3. Once the LPs are advanced, curvature κ_{LP} is evaluated using the procedure outlined in the previous section. M_4'-kernel based interpolations are performed from the LPs to the background mesh to obtain curvature ($\kappa_{cv}^{n+1/2}$). Similarly, $\Theta_{cv}^{n+1/2}$ is obtained through interpolations and $\rho_{cv}^{n+1/2}$, and $\mu_{cv}^{n+1/2}$ are calculated from equations (4). The face-based surface tension force is then obtained as:

$$F_{\sigma,f}^{n+1/2} = \sigma \kappa_f^{n+1/2} \frac{\Theta_{icv2}^{n+1/2} - \Theta_{icv1}^{n+1/2}}{|s_n|} \tag{6}$$

where s_n is the vector joining the control volumes $icv1$ to $icv2$.

4. The remaining steps are based on a variant of the co-located fractional step method [21]. We present the semi-descretization here for completeness. First, a projected velocity field $\hat{u}_i$ at the *cv*-centers is calculated:

$$\frac{\hat{u}_i - u_i^n}{\Delta t} = g_i + \frac{1}{\rho_{cv}^{n+1/2}} \left(-\frac{\partial p}{\partial x_i}^{n-1/2} + F_{v,i}^{n+1/2} + F_{\sigma,i}^{n+1/2}\right) \tag{7}$$

where $F_{v,i}$ represents the viscous, $F_{\sigma,i}$ the surface tension, and g_i the gravitational forces at the *cv* centroids. The viscous terms are treated implicitly using second order symmetric discretizations and the surface tension force is treated explicitly. The *cv*-based surface tension force is obtained from $F_{\sigma,f}$ using area weighted least-squares interpolation consistent with the pressure reconstruction scheme developed by Mahesh *et al.* [21]. This is the essence of the balanced force algorithm [13, 20].

5. Subtract the old pressure gradient:

$$u_i^{*n+1} = \hat{u}_i + \Delta t \frac{1}{\rho_{cv}^{n+1/2}} \frac{\delta p}{\delta x_i}^{n-1/2} \tag{8}$$

6. Obtain an approximation for the face-based velocity:

$$U_f^{*n+1} = \overline{u_i^{*n+1}} - \Delta t \left(\overline{\frac{F_i^{n+1/2}}{\rho_{cv}^{n+1/2}}} - \frac{F_{\sigma,f}^{n+1/2}}{\rho_f^{n+1/2}} \right) \tag{9}$$

where $\rho_f^{n+1/2} = (\rho_{icv1}^{n+1/2} + \rho_{icv2}^{n+1/2})/2$ and the interpolation operator, $\overline{\eta} = n_{i,f}[\eta_{icv1} + \eta_{icv2}]/2$, yields a face-normal component from the adjacent *cv*s and the face normal $n_{i,f}$.

7. Solve the variable coefficient Poisson equation to obtain pressure:

$$\frac{1}{\Delta t} \sum_{\text{faces of cv}} U_f^{*n+1} A_f = \sum_{\text{faces of cv}} \frac{1}{\rho_f^{n+1/2}} A_f \frac{\delta p}{\delta n}^{n+1/2} \tag{10}$$

where A_f is the face area.

8. Reconstruct the pressure gradients at the *cv* centers from the face-centers using the density-weighted face-normal gradients together with the *same* area-weighted least-squares minimization approach [21] used for the surface tension force above. The *cv* center velocities are then corrected to satisfy the continuity equation.

9. Interpolate the velocity field $u_{i,cv}^{n+1/2}$ to the LP locations and advance the LPs to the next time level.

2.2 Validation Studies for Resolved Simulations

In this section, some numerical examples of standard test cases using the above scheme are presented. First, the accuracy of the pure Lagrangian advection approach is evaluated by performing standard test cases such as the Zalesak disc rotation and the evolution of a circular interface in a deformation field [24]. These showed comparable results with published data [16] (not shown here). The following test cases are presented: (i) accuracy of the surface normal and curvature evaluation procedure for a circular interface, (ii) zero-gravity stationary bubble in a quiescent environment to investigate the level of spurious currents obtained due to errors in surface tension force representation, (iii) damped surface waves and oscillating liquid column, (iv) Rayleigh-Taylor instability, and (v) rising bubbles under gravity.

Case 1: Estimation of Surface Normal and Curvature: The accuracy of the surface normal and curvature calculation by using the procedure described before is tested on a circular interface. The Lagrangian points (LPs) are uniformly distributed in a narrow band around the interface and initialized by *exact* signed distance function. The surface normals and curvatures are first calculated on the LPs. Only those LPs are considered where $|\Phi| \leq 2\Delta_{LP}$, where Δ_{LP} is the LP-spacing. The average relative error in surface normal calculation is shown in Figure 3a indicating second order convergence. For all these LPs, corresponding points on the interface are calculated using the normals and signed distance function (Φ). The interface-projected curvature values at the interface points are evaluated using the M_4'-kernel interpolation from the neighboring LP values. These curvatures are then compared with the exact curvature ($\kappa_{exact} = 1/R$) for a two-dimensional interface. The corresponding L_1-errors are plotted at different LP-resolutions in Figure 3b, showing second order convergence.

Case 2: Static Bubble in Equilibrium: To validate the curvature and surface tension force calculation, a test of static bubble in a quiescent medium with zero gravity is considered. The pressure gradient across the interface balances the surface tension force resulting a zero velocity and static bubble at all times. Errors in representation of the surface tension and curvature at the interface, however, lead to non-zero velocity, or the so called 'spurious currents'. The exact solution for the pressure jump across the interface for a circular two-dimensional bubble is:

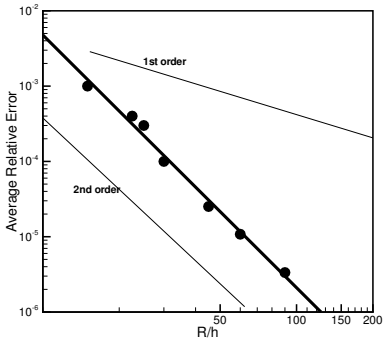

(a) Normal

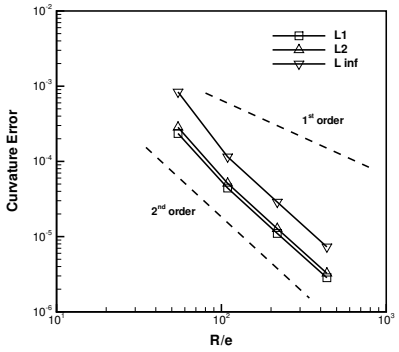

(b) Curvature

Figure 3: Error versus grid spacing for circular interface: (a) average relative error in surface normal, (b) absolute error in curvature–circles indicate error at LP location, squares indicate error at interface location.

$\Delta P_{exact} = \sigma\kappa_{exact}$ where $\kappa_{exact} = 1/R$ and R is the radius of the bubble. We consider a square domain having sides of eight units. A bubble of radius $R = 2$ is placed at the center of the domain. The surface tension coefficient σ is taken to be 73, the bubble density is 0.1 and the surrounding fluid density is 1. Accordingly, the pressure jump across the interface should be $\Delta P = 36.5$ units. All parameters are in SI units [20]. The background grid consists of uniform Cartesian elements with resolution of $R/\Delta = 10$. The resolution of the Lagrangian points is refined successively to have $R/\Delta_{LP} = 45, 60, 75$. The time step is fixed at $\Delta t = 10^{-3}$. The interface remains a perfect circle after $t = 0.5$ with low magnitudes of spurious currents. Pressure drop across the bubble is also accurately predicted (not shown here). Table 1a shows the convergence of L_1-error in total kinetic energy at $t = 0.5$, indicating second order convergence. Remeshing and reinitialization are *suppressed* in the above calculations.

Case 3: Bubble/Droplet Oscillation: Simulation of oscillating droplet or liquid column due to perturbations on the surface under zero-gravity conditions are performed to analyze the accu-

Table 1: L_1 error in the total kinetic energy for a static bubble.

Δ	0.044	0.033	0.0266
Error	4.5×10^{-8}	1.27×10^{-8}	4.09×10^{-9}

racy of the solver for capillary waves. A cylindrical liquid column with the radius perturbed according to, $r = r_0 + \alpha\cos(n\theta)$, and has a frequency of oscillation given by $\omega_n^2 = \frac{(n^3-n)\sigma}{(\rho_d+\rho_e)r_0^3}$, where ρ_d and ρ_e are the density, interior and exterior to the liquid column, respectively [6]. The cases considered include $\sigma = 1$, $\alpha = 0.01$ and 0.1 (this is 10% larger than the perturbation considered in [6]), $\rho_d = 1$, $\rho_e = 0.01$, $r_0 = 2$ in a $[-10,10]^2$ doubly connected computational domain. The grid resolution is 32^2 and the Lagrangian particle resolution is fixed at $\frac{\Delta}{\Delta_{LP}} = 4.5$. The second, third, and fourth modes are simulated. The relative error in period of oscillation $E_{period} = |T_{numerical}\omega_n/2\pi - 1|$ is given in Table 2. The errors are comparable to those reported in [6] for $\alpha = 0.01$. Stable solutions were also obtained even for ten-times larger perturbations. Similar level of accuracy in predictions were obtained for *three-dimensional* bubble oscillations (not shown for space).

Table 2: Error in predicted period of an oscillating liquid column.

Mode	Predicted ω	Theoretical ω_n	E_{period}
2	0.844	0.866	0.02
3	1.671	1.726	0.0328
4	2.58	2.719	0.0519

Case 4: Damped Surface Waves: Small amplitude damped surface wave between two immiscible fluids is investigated by comparing the numerical solution to the theoretical solution of the initial value problem obtained by Prosperetti [25]. Initially the interface between the two fluids inside a box $[0\ 2\pi]\times[0\ 2\pi]$ is perturbed by a sinusoidal wave disturbance of wavelength $\lambda = 2\pi$ and amplitude $A_0 = 0.01\lambda$ [13]. Periodic boundary conditions are used in the x direction, and slip conditions are used in the y-direction. The case analyzed consists of two fluids of equal density $\rho_1 = \rho_2 = 1$, and equal kinematic viscosities $\nu = 0.006472$. For $\sigma = 2$ and $\Delta t = 0.02$, the time-evolution of the amplitude of the surface is plotted in figure 4. Two different grid resolutions 16^2 and 32^2 are used for this test case with the $\frac{\Delta}{\Delta_{LP}} = 4$. With grid refinement, converging results are obtained compared to the analytical solution.

Case 5: Rayleigh Taylor Instability: A common test case of heavier fluid over a lighter fluid giving rise to Rayleigh-Taylor instability is performed to evaluate the accuracy of the scheme [26]. The simulation parameters are: $\rho_1 = 1.225$, $\mu_1 = 0.00313$ (heavy fluid), $\rho_2/\rho_1 = 0.1383$, $\mu_2/\mu_1 = 1$, $g = 9.81$, $\sigma = 0$ in a computational domain of size $[1,4]$. Initially the interface between the two fluids (at the center of the domain) is perturbed by a cosine wave of amplitude 0.05. The heavier fluid falls due to gravity, giving rise to a Rayleigh-Taylor instability of the interface perturbation. The surface tension forces are neglected. The boundaries in the x direction are assumed periodic whereas slip conditions are employed in the y direction. The time step is fixed at 5×10^{-4} and the flow evolutions for different grid resolutions are compared at certain time instances. The grid resolutions used are $\Delta = 1/64$, $1/128$, and $1/192$. The *LP* resolution relative to the grid is fixed at $\frac{\Delta}{\Delta_{LP}} = 4$. Figure (5a) shows the temporal evolution of the interface. Also shown is the evolution of the bubble top and spike front positions compared with the front tracking scheme [27]. The interface positions are nearly identical for all resolutions; however, the coarse grid simulation ($\Delta = 1/64$) was not able to resolve the thin filaments observed at $t = 0.9$ s.

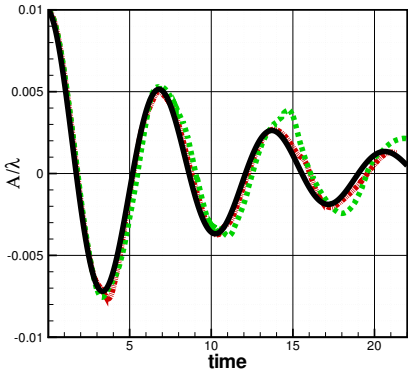

Figure 4: Time evolution of a damped surface wave for two grid resolutions $\Delta = 16^2$ (red dashed) and 32^2 (green dash dot) compared with theoretical result (black solid).

Case 6: Rising Bubbles: Lastly, we consider the rise of an air bubble column in water under gravity [28]. The computational domain is $[-0.01\ 0.01]\times[0\ 0.03]$ in the $x-y$ direction with no-slip wall conditions on the edges. A bubble of diameter $2/300$ is initially released from a distance of 0.01 from the bottom wall. The fluid properties of air and water are: $\rho_a = 1.226$, $\rho_\ell = 1000$, $\mu_a = 1.78\times10^{-5}$, $\mu_\ell = 1.137\times10^{-3}$, $\sigma = 0.0728$ and $g = 9.81$ in SI units.

Time evolution of the small bubble column is shown in Figure 6. The simulation was performed on a 80×120 grid with $\frac{\Delta}{\Delta_{LP}} = 4$. This corresponds to the finest grid used by Kang *etal.* [28] and the results are in good agreement with their predictions [28] as well as the volume-of-fluid approach [20]. The total volume loss at $t = 0.05$ was less than 0.8% for the bubble.

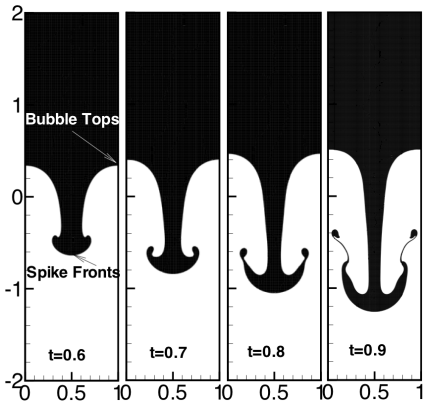

(a)

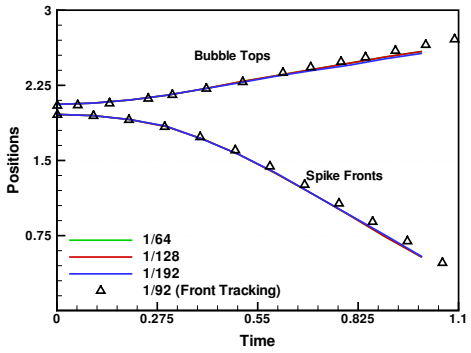

(b)

Figure 5: Rayleigh-Taylor instability: temporal evolution of (a) the interface on fine grid (1/192); (b) the bubble top and spike front positions from bottom wall compared with the front-tracking scheme [27].

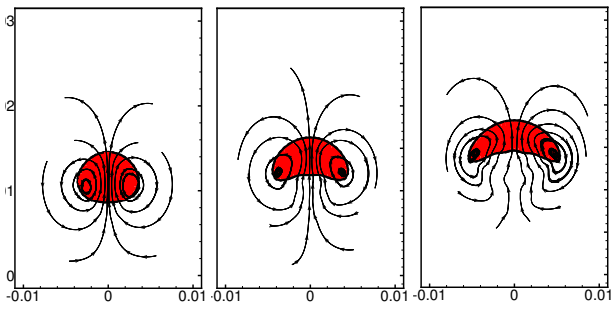

Figure 6: Time evolution of a small bubble rising under gravity: (a) t=0.02, (b) t=0.035, (c) t=0.049 s

3 DISCRETE BUBBLE MODELING

Two approaches are widely used to compute the hydrodynamics of under-resolved bubbly flows: the Euler-Euler and Euler-Lagrange. The Euler-Euler model employs the volume or ensemble averaged mass and momentum conservation equations to describe the time dependent motion of both phases [29]. In the Eulerian-Lagrangian approach, a continuum description is used for the liquid phase with discrete Lagrangian tracking of the bubbles. The bubbles are usually modeled as spherical point-particles with models for fluid-bubble interaction forces and bubble-bubble interactions [4, 30]. Such an approach has been used for turbulent bubbly-channel flows for computation of drag reduction [31], cavitation inception studies with bubble dynamics modeled using the Rayleigh- Plesset equation [32, 33].

In this work, a Euler-Lagrange approach based on the mixture-theory is used wherein the bubble-fluid interactions are captured through inter-phase momentum exchange as well as variations in local fluid void fractions. The governing equations, the numerical algorithm and relevant validation test cases are described briefly.

3.1 Bubble Dynamics

The motion of each individual bubble is computed by solving the equations of motion in a Lagrangian frame. The bubble size variations are modeled by the incompressible Rayleigh-Plesset equations. The position, momentum equations and bubble radius equations are given as:

$$\frac{\mathrm{d}}{\mathrm{dt}}(\mathbf{x}_b) = \mathbf{u}_b \tag{11}$$

$$m_b \frac{\mathrm{d}}{\mathrm{dt}}(\mathbf{u}_b) = \sum \mathbf{F}_b \tag{12}$$

$$\rho_\ell \left[R_b \frac{d^2 R_b}{dt^2} + \frac{3}{2}\left(\frac{dR_b}{dt}\right)^2 \right] = p_B - p_\infty - \frac{2\sigma}{R_b} - \frac{4\mu_\ell}{R_b}\frac{dR_b}{dt} \tag{13}$$

where $\mathbf{x}_b$ and $\mathbf{u}_b$ are the bubble position and velocity, m_b is the mass, $\sum \mathbf{F}_b$ is the total force acting on the bubble, R_b is the bubble radius, p_B and p_∞ are the pressures inside and outside of the bubble, σ is the surface tension coefficient, and μ_ℓ and ρ_ℓ are the liquid viscosity and densities, respectively. To estimate p_B, it is typically assumed that the bubble contains some contaminant gas which expands or contracts according to adiabatic or isothermal processes [34, 35]. The bubble inside pressure consists of contribution from the gas pressure p_g and the vapor pressure p_v. The net force acting on each individual bubble is given as [36]:

$$\sum \mathbf{F}_b = \mathbf{F}_G + \mathbf{F}_P + \mathbf{F}_D + \mathbf{F}_L + \mathbf{F}_{AM} + \mathbf{F}_{coll} + \mathbf{F}_{\dot{R}_b} \tag{14}$$

where $\mathbf{F}_G = (\rho_b - \rho_\ell)V_b\mathbf{g}$ is the gravitational force, $\mathbf{F}_P = -V_b\nabla p$ is the pressure force due to far-field pressure gradients, $\mathbf{F}_D = -\frac{1}{2}C_D\rho_\ell\pi R_b^2|\mathbf{u}_b - \mathbf{u}_\ell|(\mathbf{u}_b - \mathbf{u}_\ell)$ is the drag force,

$\mathbf{F}_L = -C_L \rho_\ell V_b (\mathbf{u}_b - \mathbf{u}_\ell) \times \nabla \times \mathbf{u}_\ell$ is the lift force, $\mathbf{F}_{AM} = -\frac{1}{2}\rho_\ell V_b \left(\frac{D\mathbf{u}_b}{Dt} - \frac{D\mathbf{u}_\ell}{Dt} \right)$ is the added mass force, and $\mathbf{F}_{coll}$ is the inter-bubble or bubble-wall collision forces. The force $\mathbf{F}_{\dot{R}} = -4\pi\rho_\ell R_b^2 (\mathbf{u}_b - \mathbf{u}_\ell) \frac{dR_b}{dt}$ represents momentum transfer due to variations in bubble size. Here, V_b is the bubble volume, the subscripts 'b' and 'g' correspond to the bubble and the fluid, respectively. Several different models for the drag (C_D) and lift (C_L) coefficients have been used that account for bubble deformation and variations in bubble Reynolds numbers ($Re_b = \rho_\ell |\mathbf{u}_b - \mathbf{u}_\ell| 2R_b/\mu_\ell$) [4]. Inter-bubble and bubble-wall interaction forces can be computed using the standard collision models typically used in the discrete element method [37].

The equations for the fluid phase are obtained by making use of the mixture theory. In this formulation, the volume occupied by the bubble in a fluid control volume is accounted for by computing the local bubble (Θ_b) and fluid void fractions Θ_ℓ (such that $\Theta_b + \Theta_\ell = 1$). The continuity and momentum equations account for local changes in void fractions. The continuity equation is given as:

$$\frac{\partial}{\partial t}(\rho_\ell \Theta_\ell) + \bigtriangledown \cdot (\rho_\ell \Theta_\ell \mathbf{u}_\ell) = 0 \tag{15}$$

The local spatio-temporal variations of bubble concentration, generate a non-divergence free velocity field.

$$\nabla \cdot \mathbf{u}_\ell = -\frac{1}{\rho_\ell \Theta_\ell} \frac{D\rho_\ell \Theta_\ell}{Dt} \tag{16}$$

where $\frac{D}{Dt}$ is the material derivative. Lagrangian quantities, such as bubble concentration, are interpolated to the Eulerian control volumes effectively, using the following interpolation function,

$$\Theta_b(\mathbf{x}_{cv}) = \sum_{b=1}^{N_b} V_b \mathcal{G}_\Delta(\mathbf{x}_{cv}, \mathbf{x}_b) \tag{17}$$

where $\mathcal{G}_\Delta$ is the interpolation function, N_b is the total number of bubbles, and the summation is over all bubbles. The momentum conservation equation is given as:

$$\frac{\partial}{\partial t}(\rho_\ell \Theta_\ell \mathbf{u}_\ell) + \nabla \cdot (\rho_\ell \Theta_\ell \mathbf{u}_\ell \mathbf{u}_\ell) = -\nabla(p) + \nabla \cdot (\mu_\ell \mathbf{D}) + \mathbf{f} \tag{18}$$

where p is the pressure, $\mathbf{D} = \nabla \mathbf{u}_\ell + \nabla \mathbf{u}_\ell^{\mathrm{T}}$ is the deformation tensor, and $\mathbf{f}$ is the reaction force from the bubbles on to the fluid phase per unit mass of fluid. This is obtained by using a Lagrangian-Eulerian interpolation (consistent with the void fraction computation, equation 17) of the total force $\sum \mathbf{F}_b$ on the bubble (equation 14).

For large-eddy simulation, the above equations are spatially filtered using density-weighted Favre averaging [3] and the unclosed subgrid-scale stresses are modeled by a dynamic Smagorinsky model. The liquid viscosity μ_ℓ must be changed to $\mu_{eff} = \mu_\ell + \mu_T$ accounting for the eddy viscosity. Notice that the bubble momentum equation consists of a pressure force $\mathbf{F}_P$, which when transferred to the Eulerian field contributes to a pressure-gradient based force given by $+\Theta_b \nabla p$. This force is generally combined with the pressure gradient term in the fluid momentum equation, to get $-(1-\Theta_b)\nabla p = -\Theta_\ell \nabla p$. In the absence of any fluid velocity, but in the presence of bubbles, the pressure gradient force is then appropriately balanced by the gravity force. Numerical implementation of the reaction term due to the pressure force $\mathbf{F}_P$ can then be coupled implicitly by using -$\Theta_\ell \nabla p$ in the fluid momentum equation; or can be kept as explicit wherein the fluid momentum equation is solved in the above form (equation 18) with the inter-phase force $\mathbf{f}$ consisting of contributions given in equation 14 [37]. In the test cases presented below, both approaches provided similar solutions.

3.2 Algorithm for Subgrid Bubble Dynamics

The coupled ordinary-differential equations for the subgrid-bubbles are solved first. The fluid-phase equations are solved using a pressure-based scheme for variable-density (due to void fraction variations), low-Mach number formulation as described below. The bubble-fluid interaction forces are treated explicitly.
Bubble-Phase Solution: The equation for bubble radius variations (equation 13) can be cast into two first order ODEs [31]:

$$\frac{dR_b}{dt} = y; \quad \frac{dy}{dt} = -\frac{3y^2}{2R_b} + \frac{p_B - p_\infty - 2\sigma/R}{\rho_\ell R_b} - \frac{4\mu_\ell y}{\rho_\ell R_b^2}. \tag{19}$$

This can be written in a matrix notation $[X]' = [F]$ where $[X]'$ and $[F]$ are 2×1 matrices. Following the above notation, a blended scheme can be derived:

$$[X]^{n+1} = [X]^n + h\left(\theta[F]^n + (1-\theta)[F]^{n+1}\right) \tag{20}$$

where h is the step size, n and $n+1$ denote the current and next time steps, respectively. The blending parameter (θ) can be changed between 0 and 1 to change the scheme from fully implicit to fully explicit. Using the Taylor expansion series and linearizing the right hand side matrix,

$$[X]^{n+1} = \{1 - h(1-\theta)[J]^n\}^{-1} \{h[F]^n + (1 - h(1-\theta)[J]^n)[X]^n\} \tag{21}$$

where $[J]$ is the Jacobian matrix calculated at time step n. In presence of large variations in the outside pressure (P_∞), the bubble radius (R_b) and $\frac{dR_b}{dt}$ can change rapidly. Use of a simple explicit scheme with very small time-step can be prohibitively expensive even for a single bubble computation. An adaptive time-stepping

strategy is necessary such that the bubble collapse and rapid expansion regions utilize small time-steps, but a much larger time-step can be used for relatively slow variations in bubble radius. Here an adaptive time step algorithm using the stability criteria of the solution is developed. The stability criterion is based on the eigenvalues of the linearized ODE:

$$[X]' = [J][X]; \quad [X]^{n+1} = [A]^n [X]^n, \tag{22}$$

where $[A]^n = \{1 - h(1-\theta)[J]^n\}^{-1}(1 + h\theta[J])$. This equation can be diagonalized to give

$$[Z]^{n+1} = [\lambda]^n [Z]^n \tag{23}$$

where λ is the matrix of eigenvalues $\lambda_1 =$ and λ_2 associated with R_b and dR_b/dt respectively. The solution of equation 23 is of the form: $Z_1^n = e^{\lambda_1} Z_1^0$ and $Z_2^n = e^{\lambda_2} Z_2^0$. The adaptive time-stepping strategy here is therefore, to keep the magnitude of λ_1 and λ_2 close to 1. This λ calculation is used to correct the time step if its deviation from 1 is more than 5%. This strategy is found to be very effective even in the case of rapid pressure variations as shown in the validation cases. The time-step (δt_{bub}) obtained based on the above strategy is compared with the flow-solver time-step (δt_{solver}). For the bubble position and the velocity field the same time-steps are used. A sub-cycling procedure is used, wherein the bubble time-step is maintained *five*-times smaller than the flow-solver time-step, and the bubble dynamics equations are solved repeatedly until we reach one δt_{solver}. The bubble position and velocity fields are updated using a third-order Runge-Kutta scheme; the bubbles are duly transferred across processors as their positions are updated.

Fluid Phase Solution: The numerical scheme for unstructured, arbitrary shaped elements [3] is modified to take into account the fluid void fraction. The changes in local fluid volume fractions requires solution of a *variable density* flowfield as opposed to the constant density, incompressible flows studied in [2,21]. The steps in solving the coupled fluid-particle equations are given below. A semi-implicit scheme is used for the fluid solver, however, the interphase momentum exchange terms are treated explicitly.

Step 1: Advance the bubble positions, velocities, and radii using the adaptive time-stepping algorithm described above. Compute the void fraction field at the new bubble locations and set the density $\rho = \rho_\ell \Theta_\ell$.

Step 2: Advance the fluid momentum equations using the fractional step algorithm, with the interphase force, **F**, treated explicitly (the subscript ℓ for fluid phase is dropped for simplicity).

$$\frac{\rho u_i^* - \rho u_i^n}{\Delta t} + \frac{1}{2V_{cv}} \sum_{\text{faces of cv}} \left[u_{i,f}^n + u_{i,f}^*\right] g_N^{n+1/2} A_f =$$

$$\frac{1}{2V_{cv}} \sum_{\text{faces of cv}} \mu_f^* \left(\frac{\partial u_{i,f}^*}{\partial x_j} + \frac{\partial u_{i,f}^n}{\partial x_j}\right) A_f + F_i^n$$

where f represents the face values, N the face-normal component, $g_N = \rho u_N$, and A_f is the face area.

Step 3: Interpolate the velocity fields to the faces of the control volumes and consider the corrector step:

$$\frac{\left(\rho u_i^{n+1} - \widehat{\rho u_i}\right)}{\Delta t} = -\frac{\delta p}{\delta x_i} \tag{24}$$

$$\frac{\left(\rho_f u_N^{n+1} - \widehat{\rho_f u_N}\right)}{\Delta t} = -\frac{\delta p}{\delta x_N}, \tag{25}$$

where $\hat{u}_N = \hat{u}_{i,f} n_{i,f}$ is the approximation for face-normal velocity and $n_{i,f}$ are the components of the face-normal. The face-based density ρ_f is obtained by arithmetic average of the adjacent control volume-based densities. The face-normal pressure gradient $\frac{\delta p}{\delta x_N}$ and the gradient in pressure at the cv-centroids are related by the area-weighted least-squares interpolation [3,21].

Step 4: The Poisson equation for pressure is obtained by taking the divergence of the face-normal velocity component in the above step to obtain

$$\nabla^2 (p \delta t_{solver}) = \frac{1}{V_{cv}} \sum_{\text{faces of cv}} \rho_f \widehat{u}_{i,f} A_f + \frac{\delta \rho}{\delta t_{solver}}. \tag{26}$$

Step 5: Reconstruct the pressure gradient, compute new face-based velocities, and update the cv-velocities using the least-squares interpolation [3,21]:

3.3 Validation Studies for Subgrid Bubble Dynamics

The above numerical scheme is applied to different test cases in order to evaluate its accuracy. These test cases are described below.

Case 1: Oscillating bubbles: The importance of volumetric displacement effect on the flow field, caused by change in local concentration of bubbles was investigated in this test case. The variable density formulation used in these simulations accounts for changes in the local mixture density caused by bubble accumulation/scattering in the flow field due to inter-phase momentum exchanges, or size variation in a cavitating bubble due to hydrodynamic pressure of the flow. A simple case of imposed oscillation on the radius of a bubble causing a potential flow field around itself is first simulated. This phenomenon can not be simulated by only using the inter-phase momentum coupling (neglecting variations in the void fractions). Here it is shown that the local variations in mixture density in momentum and continuity equation provide the correct solution.

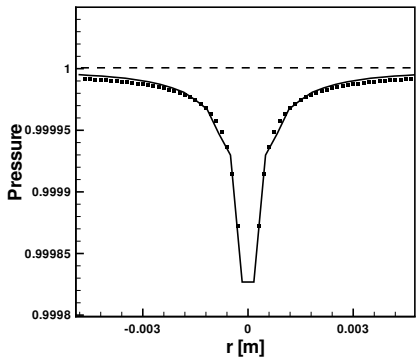

(a) Pressure Distribution

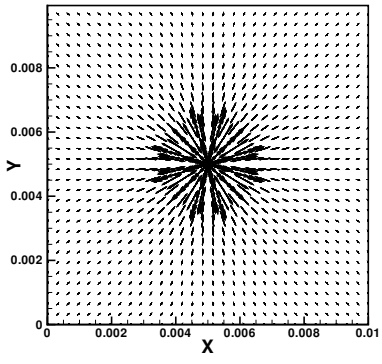

(b) Vector Field

Figure 7: Flow developed by an oscillating bubble: (a) Pressure distribution caused by volume displacement around the bubble compared with analytical solution (dashed line shows the pressure field if the void fraction variations are neglected), (b) instantaneous velocity vector field due to bubble oscillations.

A single air bubble is placed in water inside a cubical domain. A sinusoidal perturbation is imposed on the bubble. Bubble radius changes in time as $R_b = R_{b,0} + \varepsilon \sin(\omega t)$, where R_b and $R_{b,0}$ are the instantaneous and the initial radius, respectively, ε is the perturbation magnitude, ω is frequency and t is time. In this simulation, $R_0 = 0.01 \times D$, where D is the cube size, and gives overall concentration of 4×10^{-6}, $\varepsilon = 0.1 \times R_{b,0}$, $\omega = 50$ [Hz]. Figure 7a shows the radial distribution of hydrodynamic pressure around the bubble created by the size variation at $t^* = 0.3$ where $t^* = t/T$ and $T = 2\pi/\omega$. Also shown are the instantaneous velocity vectors due to bubble oscillation (Figure 7b). The pressure field is well predicted by the present numerical scheme.

In another example two bubbles oscillating in tandem are considered. Two similar bubbles are put in a box and their radius changes sinusoidally as above with a phase difference of π [rad]. All properties are similar to the case of single bubble case, except they are both located $D/6$ away from the box center. The result is a doublet-like flow which is shown in figure 8.

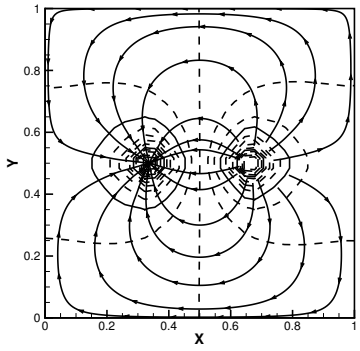

Figure 8: Doublet generated by bubbles oscillating in tandem. Streamlines and pressure contours (dashed line) are shown.

Case 2: Bubble Dynamics Under Imposed Pressure Variations:

To test the adaptive time-stepping approach, a numerical test case is considered wherein the external pressure is specified as a function of time and the bubble radius is computed using the Rayleigh-Plesset equation. This test case was also used by Qin *et al.* [31] in their work on simulating cavitating bubbles in a convergent divergent nozzle. Figure 9a shows an imposed pressure variation to a stationary bubble. The fluid properties are those for water ($\rho_\ell = 1000$ kg/m^3, $\mu_\ell = 0.798 \times 10^{-3}$ kg/ms, $\sigma = 0.072$ N/m, $p_v = 0.00424$ MPa). A bubble of initial radius ($R_{b,0} = 100$ μm, $dR_{b,0}/dt = 0$) is subjected to the outside pressure variation shown in figure 9a. The bubble undergoes growth and collapse as the outside pressure decreases and increases with time. Rapid accelerations and variations in bubble radius are observed. This test case is challenging for a numerical scheme based on constant time-steps. For an explicit Euler scheme, for example, a constant time-step on the order of 10^{-17} s would be required to capture the bubble growth and collapse and maintain a stable solution. Multiple periods of bubble oscillation would be very time-consuming for such an approach and adaptive time-stepping is essential. Figure 9b shows the solution obtained from the adaptive time-stepping. Also shown are the temporal variations in the eigenvalues λ_1 and λ_2 of the the coupled system of equations 22. Deviation of these eigenvalues from a value of unity correspond to rapid growth or decay period of the bubble and are good indicators for adaptive time-stepping. The time-step is thus changed if the eigenvalues depart from the unity value by 5% or more. With this approach stable solutions are obtained for much higher time-steps and multiple periods of bubble oscillation can be easily computed. Figure 9c shows that only around 2000 iterations are required to compute five periods of bubble oscillation. A time-step refinement study provided little variations in the predicted variations for bubble radius.

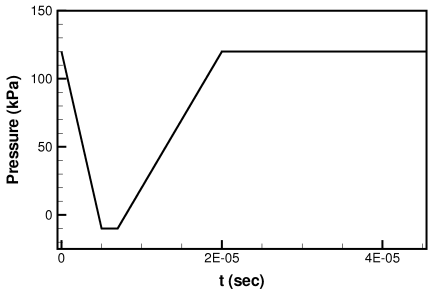

(a) Imposed outside pressure

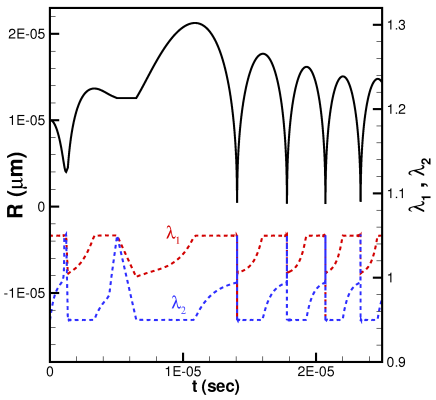

(b) $R(t), \lambda_1(t), \lambda_2(t)$

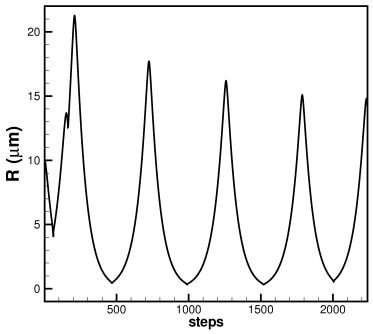

(c) Number of iterations

Figure 9: Time variation of bubble radius and λ values for a cavitating bubble with imposed pressure variations.

4 BUBBLE-VORTEX INTERACTIONS

Bubble-vortex interactions are studied by simulating two flow configurations: (i) interaction of micro-bubbles with a traveling vortex tube, (ii) interaction of a single bubble with a stationary Gaussian vortex. The second case is used to compare the predictions of bubble trajectories from the fully resolved and the discrete bubble model.

Bubble Interactions with a traveling vortex tube:

Interactions of small micro-bubbles with a traveling vortex corresponding to the experiments by Sridhar and Katz [1, 38] are investigated by using the discrete bubble model as well as the fully resolved simulation. Specifically, Sridhar & Katz observed that certain large bubbles once entrained into the vortex ring, deform the ring significantly. The simulations are setup to investigate if the presented numerical schemes can capture these effects.

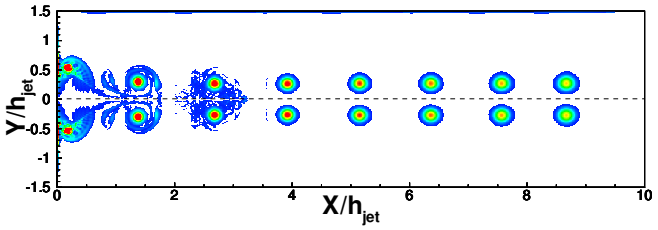

Figure 10: Vortex tube evolution and rollup visualized by out-of-plane vorticity contours. Location of bubble injection is $X/h_{jet} = 5$.

The computational domain and the evolution of the vortex tube are shown in Figure 10. There is an inflow boundary at the left wall, an outflow condition at the right boundary, and walls on the top and bottom. The total domain size is $X/h_{jet} = 10$ by $Y/h_{jet} = 3$ and is centered at $Y/h_{jet} = 0$. The inlet is modeled as an orifice rather than the piston/nozzle assembly used in the experiment. At the inlet boundary, a jet is pulsed for 0.27 seconds into the initially quiescent domain, which causes the roll up of two symmetric vortex tubes. The inflow velocity is a function of time, and is described by a sixth-order polynomial to match the experimental conditions. To keep the size of the computation small, a two-dimensional domain is simulated with periodic conditions in the spanwise direction giving rise to a vortex-tube. A uniform cartesian grid is used throughout the area below the

Table 3: Parameters for the bubble-vortex interaction.

Parameter	Value
ρ_l, ν_l	1,000 kg/m^3; 1×10^{-6} m/s^2
Domain Size	1m $\times$ 0.15m $\times$ 0.005m;
Grid Size	$800 \times 121 \times 4$
Jet height (h_{jet})	0.1 m
Inflow Time	0.27 s
Inflow Velocity	$U(t) = \sum_{n=0}^{6} a_n t^n$
a_6, a_5, a_4, a_3	62278; -47082; 13686; -2062
a_2, a_1, a_0	159.5; -1.289; 0.006

line of symmetry with a total of 800 x 121 elements in the X and Y directions. The two-dimensional domain is periodic and uses 4 grid points in the Z direction. Table 3 lists the computational parameters used in this study. After initial roll up and stabilization of the shear layer, the vortex core travels downstream with a convective velocity of 7 cm/s, which is approximately 14% of the maximum inlet velocity. The contours show the diffusion of the high vorticity in the core as the vortex tube travels downstream.

At a value of $X/h_{jet} = 5.0$, eight bubbles are injected below and in front of the vortex core. One bubble at a time is injected, with a time of $\Delta_{inj} = 10\ ms$ between each bubble. Due to buoyancy, the bubbles rise and are entrained into the vortex core. The injection point is varied so that the vortex tube encounters a rising line of bubbles as in the experiments [1]. A parametric study is performed to determine the effect of bubble buoyancy force on bubble settling location and vortex tube distortion. For comparisons with experimental data, two sets of computations are performed: (i) the bubble diameter ($2R_b$) and gravitational acceleration g are varied over a broad range, whereas the vortex strength is kept fixed, and (ii) the bubble diameter and initial vortex strengths are varied for a fixed gravitational acceleration. The later case is consistent with experimental results.

Set 1: In the first set of calculations, the bubble size is varied from 300 to 1300 μm. The strength of the initial vortex tube ($\Gamma_0 = 156$ cm/s) and the bubble injection locations remain constant for all cases. The non-dimensional parameter gR_b^3/Γ_0^2 (ratio of buoyancy force to hydrodynamic pressure gradient) ranges from 1.3×10^{-7} to 5.4×10^{-6}. The bubble Stokes number, defined as $St_b = \omega d_b^2/(36\nu)$, where $\omega = \Gamma_0/2\pi r$ has values between 0.014 and 0.264.

Set 2: In this set of calculations, the gravitational acceleration is fixed at 9.81 m/s^2. The bubble size is varied from 500 to 1300 microns, and the initial vortex strength (at the time of bubble injection) is varied from 0.025 to 0.045 m^2/s. This set of calculation represents the same parameters as used by Sridhar & Katz [1].

In all cases, each of the eight bubbles are entrained by the passing vortex tube. They rise from their release point around the rear of the vortex and are swept into the downward velocity region on the forward side of the core. Depending on the Stokes number and buoyancy force, the bubbles may circle the core multiple times before ultimately reaching their final settling location, where their average motion in the inertial reference frame is zero. The bubbles do not remain perfectly stationary in their settling location because of local variations in pressure and bubble collision forces cause slight oscillations in position. Once they have reached this state, the non dimensional settling location is averaged over all particles and in space over a distance of $5.2X/h_{jet} < X_{vx} < 5.8X/h_{jet}$. This corresponds to an averaging time of almost 1 second. This time span is similar to that used in experiments.

The non-dimensional settling location is plotted against the

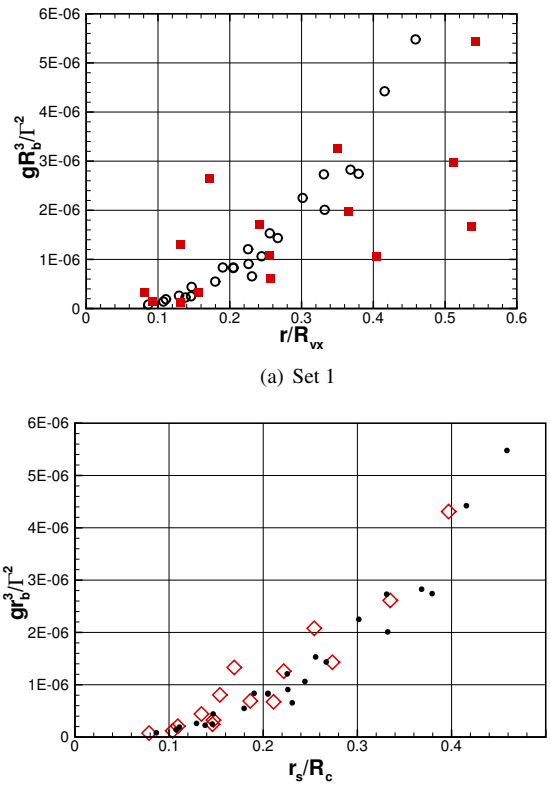

(a) Set 1

(b) Set 2

Figure 11: Comparison of the non-dimensional settling location with the experimental results of Sridhar & Katz [1]. The parameter $g(R_b)^3/\Gamma^2$ is the ratio of the buoyancy force and the hydrodynamic pressure gradient experienced by the bubble. ($\circ$) Experimental data, (filled squares) present results: (a) Set 1 runs involve fixed vortex strength but varying gravitational acceleration, (b) Set 2 runs involve fixed gravitational acceleration for different vortex strengths similar to the experiments.

non-dimensional parameter $g(R_b)^3/\Gamma_0^2$ in figures 11a,b for the discrete bubble model alongside the experimental data for the two sets of computations. For both sets of computations, the overall trends of the predicted model are consistent with the experimental data. Bubbles with small Stokes numbers and small values of gR_b^3/Γ^2 tend to move very close to the vortex core, whereas large-bubbles settle at a location further from the center of the core. More importantly, significant vortex distortion is predicted by the numerical model for certain bubbles with parameters similar to those observed in the experiments. The vortex distortion effect was found to be predominantly an effect of variations in the void fraction as the bubbles travel to their settling location. This was confirmed by computing the bubble trajectories without considering the void fraction variations. With Θ_ℓ set constant (equal to 1), vortex distortion was not obtained for

any of the cases studied. The first set of calculations (wherein the vortex strength is fixed, but gravitational acceleration is varied) show some scatter (figure 11a) when compared with experimental data; whereas the second set (wherein the gravitational acceleration is fixed, but the vortex strength is varied as in experiments) shows very good comparisons (figure 11b). This may be because of two reasons. First, the simulations involve two-dimensional vortex-tubes, whereas the experiments are three-dimensional vortex rings. Second, varying the gravitational parameter for the fixed vortex strength only affects the buoyancy force on the bubbles, the pressure gradient, drag and lift forces are relatively less impacted because the vortex strength is held fixed. When the vortex strength is varied (as in experiments), the relative magnitudes of the pressure, drag, and the lift forces are varied in a manner consistent with the experiments and the numerical results agree closely with the experiments. The instantaneous shape of the vortex core is determined by creating a map of the vorticity distribution around the vortex center. At each timestep the vorticity distribution in the vortex core is mapped onto an inertial, cylindrical coordinate system which moves with the vortex center (X_c, Y_c). This is done by discrete averaging over each grid point within the core radius. Figure 12 shows the effect of the bubble on the vortex using this mapped vorticity distribution. In the absence of the bubbles, the the vortex core is stable and the core is quite close to an oval in shape. The radial distribution (figure 12b) shows that the core has a Gaussian distribution of vorticity in the absence of bubbles. In the presence of some entrained bubbles, the vortex core deforms altering the vorticity distribution as shown by the radial and angular distributions in figure 12. This effect is attributed to the local variations in the void fractions as the bubbles are trapped inside the vortex core.

Bubble Interactions with a Gaussian vortex: Finally, to compare the fully resolved approach and the discrete bubble model, bubble trajectories inside a stationary Gaussian vortex were simulated [39]. For this two-dimensional vortex with initial circulation Γ_0 and core radius r_c, the tangential velocity is given as, $u_\theta(r) = \frac{\Gamma_0}{2\pi r}\left(1 - e^{-\eta_1 (r/r_c)^2}\right)$, where η_1 is a constant. This case is designed in such a way that the strength and other parameters of the Gaussian vortex matches with the traveling vortex tube case. Accordingly, $r_c = 0.01145$ m and $\eta_1 = 1.27$. This vortex is simulated in a domain of size $7r_c \times 7r_c \times 0.4r_c$. Two different grid sizes are used to facilitate simulations using the fully resolved and under-resolved (DBM) techniques. For the fully resolved simulation a grid of $312 \times 212 \times 60$ is used with refined grid elements within the vortex core. For the discrete bubble model, a coarser uniform grid of $64 \times 64 \times 4$ grid elements are used. The entrainment of the bubble in this vortex is simulated using both approaches. The flow parameters are: $\rho_\ell = 1000$ kg/m^3, $\rho_g = 1$ kg/m^3, $\mu_\ell = 0.001$ Pa$-$s. The gravitational acceleration g is varied for a 1200 μm bubble released at $\theta = 0$ and $r/r_c = 1.8$. Figure 13 shows comparison

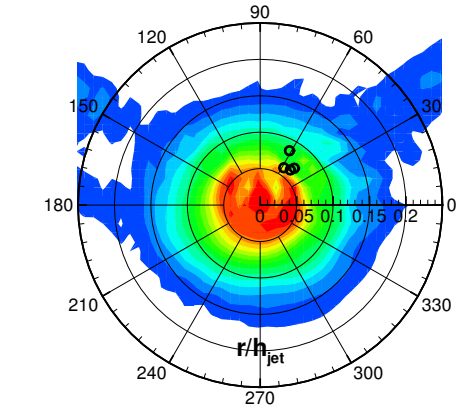

(a) Vorticity contours

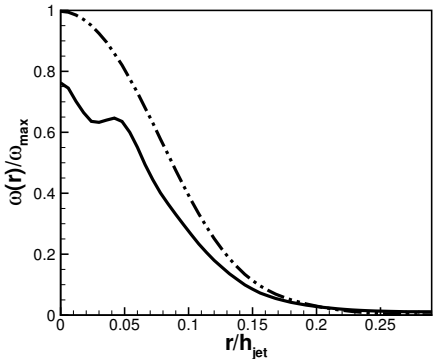

(b) Radial mapping

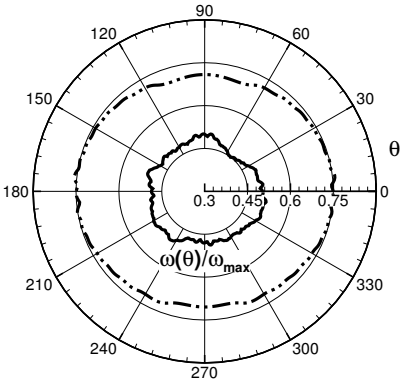

(c) Angular mapping

Figure 12: Vortex distortion by the entrained bubbles ($2R_b = 1,300\mu m$ bubbles; $g = 5m/s^2$) : (a) vorticity contours and bubble locations (black dots), (b) radial mapping of vorticity, and (c) angular mapping of vorticity. (—) with void fraction variations, (—··—) without accounting void fraction variations.

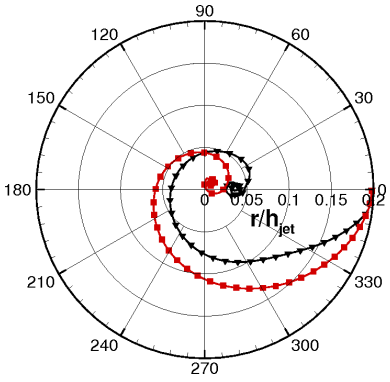

(a) $g = 3$ m/s^2

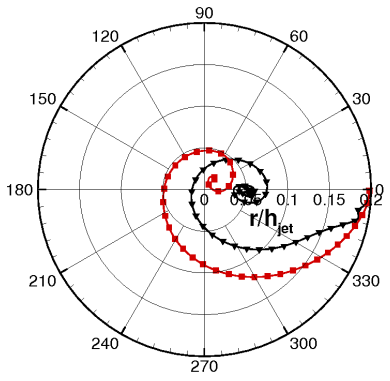

(b) $g = 5$ m/s^2

Figure 13: Comparison of the bubble trajectories predicted by fully resolved (black triangles) and discrete bubble (red squares) approaches for a bubble of diameter 1200 μm captured by a Gaussian vortex: (a) $g = 3$ m/s^2, and (b) $g = 5$ m/s^2.

of the trajectory of the bubble obtained from the fully resolved and the discrete bubble model for two different gravitational accelerations. It is observed that the bubbles spiral around the vortex and eventually settle at a point further from the center of the vortex core. The trajectories of the bubbles predicted by the two approaches are similar; though the fully resolved bubble takes a more direct route to the vortex center in both cases. The fully resolved approach captures the wake effects accurately, whereas these effects are modeled in the DBM approach. These results are consistent with those of Oweis *et al.* [39].

5 CONCLUSIONS

In this work two different numerical approaches capable of capturing the bubble dynamics at different scales depending upon the relative size of the bubbles compared to the grid resolution were developed and extensively validated against standard test cases to show good predictive capability. For fully resolved simulations, a novel approach combining a particle-based, mesh-free technique with a finite-volume flow solver, was developed. The approach uses marker points around the interface and advects the signed distance to the interface in a Lagrangian frame. The kernel–based derivative calculations typical of particle methods are used to extract the interface normal and curvature from unordered marker points. Unlike front-tracking methods, connectivity between the marker points is not necessary. For under-resolved bubbles, a mixture-theory based Eulerian-Lagrangian approach accounting for volumetric displacements due to bubble motion and size variations was developed. The bubble dynamics is modeled by Rayleigh-Plesset equations using an adaptive time-stepping scheme. A generalized criterion based on the eigenvalues of the coupled ordinary differential equations for bubble radius was developed and tested to give robust solutions for large variations in the surrounding pressure field. A detailed validation study of both approaches is performed to test the accuracy of the method on a variety of single and multiple bubble problems to show good predictive capability. The approaches were applied to study bubble-vortex interaction in a traveling vortex tube (a two-dimensional representation of a vortex ring experiment by Sridhar and Katz [1]) and a stationary Gaussian vortex [39]. It was found that the Eulerian-Lagrangian model captures the vortex deformation due to bubble motion correctly.

The above numerical approaches are developed in a parallel numerical framework [2] for large-scale simulations of bubbly flows. The fully resolved formulation was based on the assumption of incompressible fluids. For cavitating bubbly flows with dense regions of bubble clouds, further modifications addressing the pressure-velocity-and density coupling [40] can be incorporated into the present approach to account for bubble compressibility. In addition, the subgrid bubble dynamics model is applicable to cavitating flows where discrete bubbles are present without dense cloud formations. The discrete bubble model has been applied to evaluate cavitation inception in a LES study of flow over an open cavity [41].

ACKNOWLEDGMENT

This work is supported by the Office of Naval Research (ONR) grant number N000140610697, monitored by Dr. Ki-Han Kim.

REFERENCES

[1] Sridhar, G., and Katz, J., 1999. “Effect of entrained bubbles on the structure of vortex rings”. *Journal of Fluid Mechanics,* **397**, pp. 171–202.

[2] Apte, S., Mahesh, K., Moin, P., and Oefelein, J., 2003. “Large-eddy simulation of swirling particle-laden flows in a coaxial-jet combustor”. *International Journal of Multiphase Flow,* **29**(8), pp. 1311–1331.

[3] Mahesh, K., Constantinescu, G., Apte, S., Iaccarino, G.,

Ham, F., and Moin, P., 2006. "Large-Eddy Simulation of Reacting Turbulent Flows in Complex Geometries". *J. Applied Mech.,* **73**, p. 374.

[4] Darmana, D., Deen, N., and Kuipers, J., 2006. "Parallelization of an Euler–Lagrange model using mixed domain decomposition and a mirror domain technique: Application to dispersed gas–liquid two-phase flow". *Journal of Computational Physics,* **220**(1), pp. 216–248.

[5] Tryggvason, G., Bunner, B., Esmaeeli, A., Al-Rawahi, N., Tauber, W., Han, J., Jan, Y., Juric, D., and Nas, S., 2001. "A front-tracking method for the computations of multiphase flow". *J. Comput. Phys.,* **169**(2), pp. 708–759.

[6] Torres, D., and Brackbill, J., 2000. "The point-set method: front-tracking without connectivity". *J. Comp. Physics,* **165**(2), pp. 620–644.

[7] Scardovelli, R., and Zaleski, S., 1999. "Direct numerical simulation of free-surface and interfacial flow". *Annu. Rev. Fluid Mech.,* **31**(1), pp. 567–603.

[8] Sethian, J., 2001. "Evolution, implementation, and application of level set and fast marching methods for advancing fronts". *J. Comput. Phys.,* **169**(2), pp. 503–555.

[9] Osher, S., and Fedkiw, R., 2001. "Level set methods-An overview and some recent results". *J. Comput. Phys.,* **169**(2), pp. 463–502.

[10] Sussman, M., 2003. "A second order coupled level set and volume-of-fluid method for computing growth and collapse of vapor bubbles". *J. Comput. Phys.,* **187**(1), pp. 110–136.

[11] Passandideh-Fard, M., and Roohi, E., 2008. "Transient simulations of cavitating flows using a modified volume-of-fluid (VOF) technique". *International Journal of Computational Fluid Dynamics,* **22**(1), pp. 97–114.

[12] Enright, D., Fedkiw, R., Ferziger, J., and Mitchell, I., 2002. "A hybrid particle level set method for improved interface capturing". *J. Comput. Phys.,* **183**(1), pp. 83–116.

[13] Herrmann, M., 2008. "A balanced force refined level set grid method for two-phase flows on unstructured flow solver grids". *Journal of Computational Physics,* **227**(4), pp. 2674–2706.

[14] Monaghan, J., 2005. "Smoothed particle hydrodynamics". *Reports on Progress in Physics,* **68**(8), pp. 1703–1759.

[15] Koumoutsakos, P., 2005. "Multiscale flow simulations using particles". *Annu. Rev. Fluid Mech.,* **37**(1), pp. 457–487.

[16] Hieber, S., and Koumoutsakos, P., 2005. "A Lagrangian particle level set method". *J. Comput. Phys.,* **210**(1), pp. 342–367.

[17] Strain, J., 2001. "A fast semi-Lagrangian contouring method for moving interfaces". *J. Comp. Phy.,* **170**, pp. 373–394.

[18] Eldredge, J. D., Leonard, A., and Colonius, T., 2002. "A general deterministic treatment of derivatives in particle methods". *J. Comput. Phys.,* **180**(2), pp. 686–709.

[19] Brackbill, J., Kothe, D., and Zemach, C., 1992. "A continuum method for modeling surface tension". *J. Comput. Phys.,* **100**(2), pp. 335–354.

[20] Francois, M., Cummins, S., Dendy, E., Kothe, D., Sicilian, J., and Williams, M., 2006. "A balanced-force algorithm for continuous and sharp interfacial surface tension models within a volume tracking framework". *J. Comput. Phys.,* **213**(1), pp. 141–173.

[21] Mahesh, K., Constantinescu, G., and Moin, P., 2004. "A numerical method for large-eddy simulation in complex geometries". *J. Comput. Phys.,* **197**(1), pp. 215–240.

[22] Gómez, P., Hernández, J., and López, J., 2005. "On the reinitialization procedure in a narrow-band locally refined level set method for interfacial flows". *Int. J. Numer. Meth. Eng.*

[23] Fatemi, E., and Sussman, M., 1995. "An efficient interface preserving level-set re-distancing algorithm and its application to interfacial incompressible fluid flow". *SIAM J. Sci. Comput.,* **158**(1), pp. 36–58.

[24] Shams, E., and S.V., A., 2007. "A hybrid Lagrangian-Eulerian approach for two-phase flows with fully resolved interfaces". *ILASS America's* 20^{th} *Annual Conference on Liquid Atomization and Spray Systems, Chicago, IL, May 2007,* **30**.

[25] Prosperetti, A., 1981. "Motion of two superposed viscous fluids". *Phy. Fluids,* **24**(7), pp. 1217–1223.

[26] Popinet, S., and Zaleski, S., 1999. "A front-tracking algorithm for accurate representation of surface tension". *Int. J. Numer. Methods Fluids,* **30**, pp. 775–793.

[27] Terashima, H., and Tryggvason, G., 2009. "A front-tracking/ghost-fluid method for fluid interfaces in compressible flows". *Journal of Computational Physics,* **228**(11), pp. 4012 – 4037.

[28] Kang, M., Fedkiw, R., and Liu, X., 2000. "A Boundary Condition Capturing Method for Multiphase Incompressible Flow". *J. Sci. Comput.,* **15**(3), pp. 323–360.

[29] van Sint Annaland, M., Deen, N., and Kuipers, J., 2005. "Numerical simulation of gas bubbles behaviour using a three-dimensional volume of fluid method". *Chemical engineering science,* **60**(11), pp. 2999–3011.

[30] Ferrante, A., and Elghobashi, S., 2007. "On the accuracy of the two-fluid formulation in direct numerical simulation of bubble-laden turbulent boundary layers". *Physics of Fluids,* **19**, p. 045105.

[31] Alehossein, H., and Qin, Z., 2007. "Numerical analysis of Rayleigh–Plesset equation for cavitating water jets". *Int. J. Numer. Meth. Engng,* **72**, pp. 780–807.

[32] Hsiao, C., and Chahine, G., 2002. "Prediction of vortex cavitation inception using coupled spherical and non-spherical models and UnRANS computations". In Proceedings of 24th Symposium on Naval Hydrodynamics, Fukuoka, Japan.

[33] Hsiao, C., Jain, A., and Chahine, G., 2006. "Effect of Gas

Diffusion on Bubble Entrainment and Dynamics around a Propeller". In Proc, Vol. 26.
[34] Brennen, C., 1995. *Cavitation and bubble dynamics*. Oxford University Press, USA.
[35] Chahine, G., 1994. "Strong interactions bubble/bubble and bubble/flow". In IUTAM conference on bubble dynamics and interfacial phenomena (ed. JR Blake). Kluwer.
[36] Johnson, V., and Hsieh, T., 1966. "The influence of the trajectories of gas nuclei on cavitation inception". In Sixth Symposium on Naval Hydrodynamics, pp. 163–179.
[37] Apte, S., Mahesh, K., and Lundgren, T., 2008. "Accounting for finite-size effects in simulations of disperse particle-laden flows". *International Journal of Multiphase Flow*, pp. 260–271.
[38] Sridhar, G., and Katz, J., 1995. "Drag and lift forces on microscopic bubbles entrained by a vortex". *Physics of Fluids,* **7**, p. 389.
[39] Oweis, G., van der Hout, I., Iyer, C., Tryggvason, G., and Ceccio, S., 2005. "Capture and inception of bubbles near line vortices". *Physics of Fluids,* **17**, p. 022105.
[40] Senocak, I., and Shyy, W., 2004. "Interfacial dynamics-based modelling of turbulent cavitating ows, part-2: time-dependent computations". *International Journal for Numerical Methods in Fluids,* **44**, pp. 997–1016.
[41] Shams, E., and Apte, S., 2009. "Large eddy simulation of cavitation inception in a high speed flow over an open cavity". In Proceedings of the 7th International Symposium on Cavitation, CAV2009, Ann Arbor, Michigan, USA (submitted).